

LOONG: Online Time-Optimal Autonomous Flight for MAVs in Cluttered Environments

Xin Guan, Fangguo Zhao, Qianyi Wang, Chengcheng Zhao, Jiming Chen, *Fellow, IEEE*, and Shuo Li,

Abstract—Autonomous flight of micro air vehicles (MAVs) in unknown, cluttered environments remains challenging for time-critical missions due to conservative maneuvering strategies. This article presents an integrated planning and control framework for high-speed, time-optimal autonomous flight of MAVs in cluttered environments. In each replanning cycle (100 Hz), a time-optimal trajectory under polynomial presentation is generated as a reference, with the time-allocation process accelerated by imitation learning. Subsequently, a time-optimal model predictive contouring control (MPCC) incorporates safe flight corridor (SFC) constraints at variable horizon steps to enable aggressive yet safe maneuvering, while fully exploiting the MAV’s dynamics. We validate the proposed framework extensively on a custom-built LiDAR-based MAV platform. Simulation results demonstrate superior aggressiveness compared to the state of the art, while real-world experiments achieve a peak speed of 18 m/s in a cluttered environment and succeed in 10 consecutive trials from diverse start points. The video is available at the following link: <https://youtu.be/vexXXhv99oQ>.

Index Terms—Aerial robotics, obstacle avoidance, integrated planning and control, motion planning.

I. INTRODUCTION

AUTONOMOUS navigation techniques [1], [2] for micro air vehicles (MAVs) leverage onboard sensing and computation to perceive the unknown environment and plan collision-free trajectories. These capabilities have rendered autonomous MAVs increasingly indispensable in diverse applications, including aerial photography and industrial inspection [3]. Their importance is further amplified in time-critical missions such as search and rescue [4] and disaster relief [5], where timely and safe arrival is crucial. In parallel with these practical demands, autonomous MAVs have continuously broken speed records in recent years, driven by the emergence of autonomous drone racing [6], [7]. This competitive platform, with its emphasis on time-optimal performance, has become a benchmark for evaluating agile trajectory generation and robust control strategies under extremely high-speed conditions. Despite such progress, achieving time-optimal high-speed flight in real time, particularly in unknown environments, remains a formidable challenge. Specifically, the limited onboard resources of MAVs demand efficient system architectures and algorithms capable of handling complex dynamics models, unexpected disturbances and safety constraints in real time.

The authors are with the College of Control Science and Engineering, Zhejiang University, Hangzhou 310027, China (e-mail: shuo.li@zju.edu.cn) (*Corresponding author: Shuo Li*).

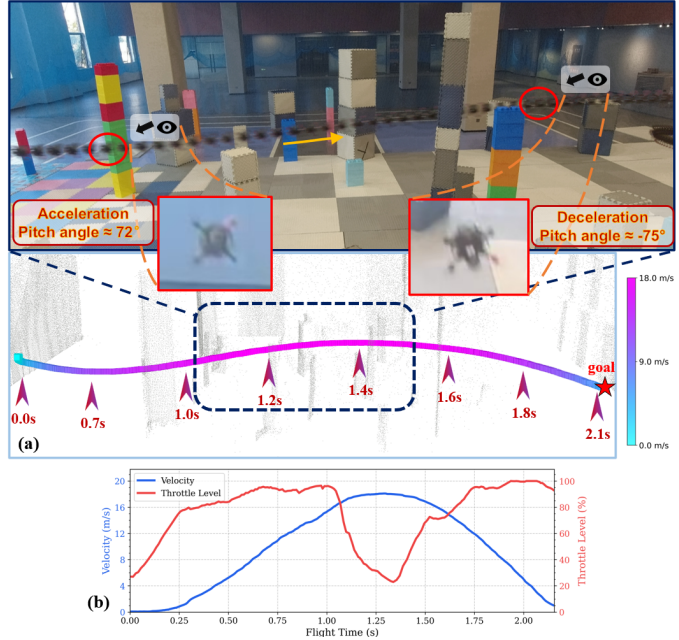


Fig. 1. (a) High-speed autonomous flight trajectory of our method in the real world and point-cloud map visualization. (b) The corresponding throttle and velocity profiles. The MAV completes a 20 m flight in 2.1 s and reaches a peak speed of 18.1 m/s in 1.2 s. Side and forward views both reveal that the MAV attains an aggressive pitch angle of approximately 75° during acceleration and deceleration.

Several works have focused on achieving online autonomous flight for MAV systems in unknown and cluttered environments. In early efforts, Richter et al. [8] achieve aggressive flights in known environments by optimizing polynomial trajectories based on differential flatness [9], [10] of the quadrotor to improve systematic efficiency. For real-time collision avoidance in unknown environments, a complete MAV system [11] is introduced based on a local polynomial trajectory planner. In [12], a MAV navigates through cluttered environments in a receding-horizon fashion, where only a local map is maintained for the local planner. In this fashion, an adequate replanning frequency is required, since high computation delays severely limit both flight speed and success rate [13]. To enable efficient replanning, Fast-Planner [14] employs B-spline for path-guided optimization, while EGO-Planner-v2 [15] leverages control effort minimizer (MINCO) [16] for spatial-temporal optimization. However, the aforementioned methods cannot systematically enable high-speed flight. One reason for such low-speed flight is that visual perception can not provide a sufficiently long detection range (typically below

5 m) and reaction time for avoiding obstacles at high speeds. A straightforward solution is to employ LiDAR sensors, which deliver a sufficiently wide sensing range. For instance, Ren et al. [17] adopt a LiDAR-based receding horizon planning to enable high-speed flight in the wild. More recently, the state-of-the-art method SUPER [13] demonstrates LiDAR-based safety-assured high-speed navigation in unknown environments using two-trajectory planning, with trajectory tracking by on-manifold MPC [18]. Even so, these methods do not address the other reason for conservative flight, namely that the separation of planning and control into a multi-stage pipeline increases system latency. To address this, integrated planning and control (IPC) methods employ model predictive control (MPC) with a point-mass model [19] or collective-thrust-input model [20] for agile obstacle avoidance. Another class of approaches is end-to-end learning frameworks, which inherently adopt an integrated pipeline. Loquercio et al. [21] apply imitation learning to enable high-speed flight in the wild with inputs of depth images and partial states. Zhang et al. [22] exploit a differentiable physics engine with a point-mass model and depth rendering to learn agile flight across diverse scenarios. Nevertheless, a substantial gap remains compared with time-optimal flights. First, when constraints exist, optimal solutions cannot in general be represented by polynomial splines [16], as used in most optimization-based frameworks. Second, mismatches between state-level constraints (on velocity/acceleration) used in the above frameworks and actual input constraints in real systems can cause tracking failure or excessive conservatism. Finally, all of the aforementioned frameworks rely on simplified dynamics rather than full dynamics, and employ conservative time allocations to satisfy real-time computational limits onboard MAVs.

In terms of time-optimal planning and control, several studies of drone racing have focused on minimizing flight time by fully exploiting the system dynamics, including the low-level actuator inputs (e.g., single-motor thrust), under the given MAV platform and maximum thrust-to-weight ratio (TWR). Remarkably, Foehn et al. optimize global trajectories through waypoints using a complementary progress constraint to achieve time-optimal planning [23]. However, such methods are computationally expensive and unsuitable for online replanning. To address this issue, reinforcement learning (RL) and model predictive contouring control (MPCC) have been introduced. Song et al. use an RL controller to reach a peak speed of 30 m/s with a maximum TWR of 12, with external computation and sensing [24]. Kaufmann et al. similarly fly the MAV at its physical limits, using the onboard camera [25]. These RL methods can learn agile flight policies, yet often suffer from limited generalization to unseen scenarios and require offline training. Time-optimal MPCC provides an integrated planning-control framework that optimizes progress along a reference path while effectively handling dynamics and disturbances, achieving a peak speed over 16 m/s with a maximum TWR of 3.3 [26]. Romero et al. propose a sample-based method to generate a point-mass model reference for MPCC [27]. Nevertheless, all these works assume a known environment (e.g., a racing track). Therefore, their integration into autonomous navigation systems and generalization

to safely traverse unknown environments, especially under limited onboard resources, remain unclear.

To handle obstacle avoidance, the distance and gradient information to obstacles, derived from Euclidean signed distance field (ESDF) [28] or from projected gradient information [15], are commonly integrated into gradient-based trajectory optimization as penalty terms. However, such gradient-based methods struggle to guarantee safety in high-speed flight, since they do not provide explicit safety boundaries for optimization. When obstacles are suddenly detected during high-speed flight, soft penalties may cause the trajectory optimization to violate constraints, potentially leading to collisions with obstacles. One class of solutions for solving this problem employs control barrier function (CBF) constraints to ensure the safety of dynamic systems by defining safe sets for quadrotor states [20]. However, while CBF provides formal safety guarantees, it can be sensitive to input limits and constraint conflicts, and often requires careful tuning to ensure feasibility and practical effectiveness. Another widely adopted approach abstracts obstacle-free spaces as convex polytopes [29], also referred to as a safe flight corridor (SFC) [30]. This compact, convex representation significantly simplifies optimization and enhances planning efficiency and reliability in cluttered environments. Nonetheless, while the aforementioned works can realize safe obstacle avoidance across diverse scenarios, their planning-control frameworks, algorithm implementations, and system integrations fail to jointly achieve the time-optimal motion performance in unknown environments.

Despite such advances, existing works do not concurrently satisfy the requirements of time-optimal, high-speed autonomous flight with safe obstacle avoidance in unknown environments for MAVs. In this paper, we propose a learning-accelerated online time-optimal integrated planning and control framework (LOONG), which builds upon our previous work in drone racing [31] and is inspired by SUPER [13]. The key contributions of this work are as follows:

- 1) A time-optimal integrated planning and control framework (Fig. 2) for MAVs is proposed to achieve autonomous flight in unknown, cluttered environments. This framework is characterized by high-frequency replanning (100 Hz). At each replanning step, time-optimal polynomial reference generation is accelerated through learning-based time allocation. Following this reference, the planning and control are solved simultaneously in one optimization problem to further enhance system performance.
- 2) An efficient MPC is proposed that integrates time-optimal MPCC with SFC for MAVs integrated planning and control, especially in high-speed flight, leveraging the MAV's full dynamics. By imposing SFC constraints at variable horizon steps, we concurrently satisfy both aggressiveness and safety requirements. The outputs of MPCC are directly used as actual execution commands.
- 3) We integrate the proposed method into a LiDAR-based fully autonomous quadrotor system and extensively evaluated the system in both simulation and real-world environments. In simulation, our framework outperformed the state of the art for autonomous navigation in terms of aggressiveness while achieving obstacle avoidance. In the

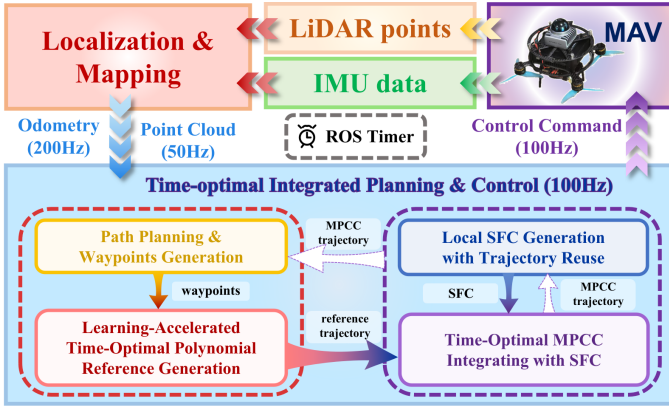


Fig. 2. LOONG is an integrated planning-control framework designed for time-optimal autonomous flight. By leveraging odometry and a point-cloud map generated from LiDAR and IMU sensors, LOONG directly outputs angular velocity and throttle commands to the flight control unit. It comprises a computationally lightweight reference generation module as the frontend, and a high-performance optimal control module as the backend. Online replanning is guided by the previous MPCC trajectory to achieve both aggressive and safe flight.

real world, the MAV achieved a peak speed of 18 m/s in a 20 m flight and succeeded over 10 consecutive trials from different start points.

II. LEARNING-ACCELERATED ONLINE TIME-OPTIMAL REFERENCE TRAJECTORY GENERATION

The system architecture based on the proposed planning and control framework is illustrated in Fig. 2. It operates upon a point-cloud map and characterized by a learning-accelerated time-optimal trajectory generator (Section II) with a processing latency below 1 ms to swiftly respond to environmental changes during high-speed flight, and a safe-enhanced time-optimal MPCC algorithm (Section III), which runs at 100 Hz.

In time-optimal autonomous flight, efficient trajectory planning is crucial for ensuring safety at high speeds due to the limited perception range. This section employs an efficient and safe front-end path planning method, along with a learning-based time-allocation approach, for reference trajectory generation. This method significantly enhances the efficiency of generating time-optimal polynomial trajectories to serve as exploratory references for MPCC, which requires a good approximation of the time-optimal policy to enhance the stability and quality of the solution.

A. Path Planning and Waypoints Generation

The front-end path planning aims to efficiently generate a safe global path including discrete positions or waypoints for obstacle avoidance from the current position p_c to the goal position p_d , as depicted in Fig. 3. Initially, an A* path (i, orange points) search algorithm is employed to find a collision-free path connecting p_c and p_d . To find the shorten path (ii), the discretized A* path is then refined by iteratively finding the furthest visible point from the end of the last line segment (blue lines).

Since the shortened path typically lies near obstacle boundaries, inspired by [13], we want to enhance safety by keeping

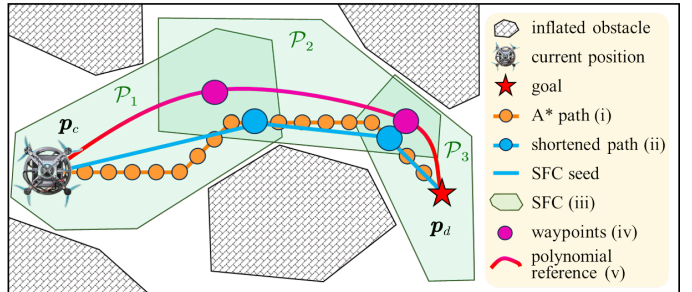


Fig. 3. Path planning and waypoints generation process involves (i) an A*-based path search, (ii) shorten and line seed generation, (iii) SFC convex decomposition (iv) and computing overlapping centers as waypoints for (v) subsequent trajectory generation.

waypoints away from obstacles, as this improves onboard sensor visibility and enlarges the free space available for local trajectory planning. To this end, we introduce the concept of a safe flight corridor (SFC), which consists of a set of convex polytopes derived from seeds (e.g., point or line) that explicitly exclude obstacles [29]. The polytope \mathcal{P} is defined as the intersection of m half-spaces:

$$\mathcal{P} = \{y \in \mathbb{R}^n \mid Ay \leq b\}, \quad A \in \mathbb{R}^{m \times n}, \quad b \in \mathbb{R}^m \quad (1)$$

where y are the states of the MAV, m is the number of hyperplanes of a convex polytope, $A \in \mathbb{R}^{m \times n}$ representing the normal vectors of hyperplanes, and $b \in \mathbb{R}^m$ representing the constants of hyperplanes. Here, we set $n = 3$ to impose SFC constraints on position space.

Therefore, as shown in Fig. 3, each line segment derived from the shortened path (ii) can serve as a seed for SFC convex decomposition (iii, green polytopes). Then, the centers of the overlapping regions between adjacent polytopes are selected as waypoints (iv, purple points) for subsequently generating time-optimal polynomial reference trajectories (v). Specifically, to enhance efficiency and ensure compatibility with LiDAR point clouds, we adopt the configuration-space iterative regional inflation (CIRI) algorithm [13], which directly operates on point clouds to extract convex polytopes.

B. Time-Optimal Polynomial Trajectory Optimization

After path planning, a sequence of next M waypoints p_i , $\forall i \in \{1, \dots, M\}$ is obtained. To enable high-speed flight, This section focuses on generating a time-optimal reference under the finite-degree polynomial representations passing through all p_i . Typically, when considering the full quadrotor dynamics, the nonlinearity of constraints make model-based time-optimal trajectory optimization computationally demanding. By exploiting the differential flatness [9], [10], the quadrotor's trajectory can be expressed through its flat outputs: $\sigma = [p_x, p_y, p_z, \psi]^T \in \mathbb{R}^3 \times S^1$, where $p = [p_x, p_y, p_z]^T \in \mathbb{R}^3$ denotes the position, and $\psi \in S^1$ indicates the yaw angle. As such, constraints can be applied discretely to the linear combination of the 0-th to s -th order derivatives of σ . To extract state information at any timestamp, a common method involves parameterizing the trajectory as a M -piece polynomial $\sigma(t)$, with each piece represented by a $N = 2s - 1$ degree polynomial $\sigma_i(t) = \mathbf{c}_i^\top \beta(t - t_{i-1})$, $t \in [t_{i-1}, t_i]$, where $\beta(t) = [1, t, t^2, \dots, t^N]^\top$.

The polynomial trajectory $\sigma(t)$ is encoded through its coefficient matrix \mathbf{c} and time allocation intervals \mathbf{T} :

$$\begin{aligned}\mathbf{c} &= [\mathbf{c}_1^\top, \dots, \mathbf{c}_M^\top]^\top \in \mathbb{R}^{2Ms \times 4} \\ \mathbf{T} &= [T_1, \dots, T_M]^\top \in \mathbb{R}_{>0}^M\end{aligned}\quad (2)$$

where T_i represents the duration of the i -th segment. The timestamp for each waypoint is given by $t_i = \sum_{j=1}^i T_j$ and the total duration of the trajectory is $T = \|\mathbf{T}\|_1$.

Using the minimal-control polynomial trajectory [16], the coefficient matrix is given by:

$$\mathbf{M}(\mathbf{T})\mathbf{c} = \mathbf{b} \quad (3)$$

where $\mathbf{M} \in \mathbb{R}^{2Ms \times 2Ms}$ is a nonsingular banded matrix determined solely by the time allocation \mathbf{T} , and $\mathbf{b} \in \mathbb{R}^{2Ms \times 4}$ contains the specified derivatives (i.e., the positions and their respective derivatives) at the boundaries of $\sigma_i(t)$.

The unique solution \mathbf{c} can be obtained by solving (3) given \mathbf{T} . Within the polynomial representation, the time-optimal trajectory generation problem is defined as:

$$\begin{aligned}\min_{\mathbf{T}} \quad & T, \\ \text{s.t.} \quad & \mathcal{F}(\sigma(t), \dots, \sigma^{(s)}(t)) \leq 0, \quad \forall t \in [0, T], \\ & \sigma^{[s-1]}(0) = \sigma_o, \quad \sigma^{[s-1]}(T) = \sigma_f, \\ & \sigma(t_i) = \sigma_i, \quad 1 \leq i \leq M-1\end{aligned}\quad (4)$$

where $\sigma_o \in \mathbb{R}^{4 \times s}$ denotes the initial state, and $\sigma_f \in \mathbb{R}^{4 \times s}$ represents the final state. σ_i represents the combination of \mathbf{p}_i and a fixed yaw angle, and \mathcal{F} represents the dynamically feasible constraints imposed on the system.

In this paper, we represent the trajectory using 5-degree minimum-jerk polynomials, with $s = 3$ to satisfy the collective thrust and bodyrates constraints. The optimization problem (4) can be solved in two layers, with the outer layer optimizing the duration T_i and the inner layer solving (3) for a given T_i to compute the coefficients \mathbf{c}_i of each polynomial segment. However, the outer layer optimization problem is non-convex, and solving it with nonlinear constraints to find feasible solutions can be computationally intensive. Furthermore, the quality and success rate of the optimization are sensitive to the initial guess of \mathbf{T} , which makes it difficult to stably generate valid trajectories. Therefore, a stable and efficient method is required to optimize time allocation and generate references for MPCC during high-frequency planning in flight.

C. Accelerating Time Allocation by Imitation Learning

As stated above, the main challenge in generating a time-optimal trajectory lies in solving the computationally intensive minimum-time problem (4), primarily due to the complexity of time allocation and the sensitivity to initial conditions. Fortunately, once the optimal time allocation \mathbf{T}^* is provided, the polynomial trajectory can be generated by solving (3) with linear complexity, requiring minimal computational resources.

To accelerate the time allocation process in real time, we utilize a lightweight neural network that mimics the time allocation of expert trajectories, as shown in Fig. 4. The network consists of a multi-layer perceptron (MLP) with two hidden layers, each containing 512 neurons. The MLP's input is a

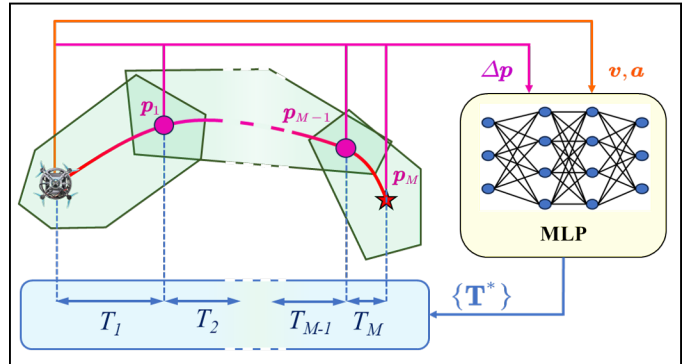


Fig. 4. Neural network inferences time allocation from current states and waypoints to efficiently generate a multi-piece polynomial as reference trajectory.

one-dimensional vector comprising the MAV's current velocity $\mathbf{v} \in \mathbb{R}^3$ and acceleration $\mathbf{a} \in \mathbb{R}^3$, along with the relative positions to the next M waypoints $\Delta\mathbf{p} \in \mathbb{R}^{3 \times M}$. The output is the sequence of optimal time allocations $\mathbf{T}^* \in \mathbb{R}^M$. Note that during flight in unstructured environments, the number of waypoints obtained by the front-end path planner may vary. To address this, we set a sufficiently large M to maintain the neural network architecture and pad the input and output with placeholder values to preserve the expected dimensions. Subsequently, the vector \mathbf{T}^* is utilized alongside \mathbf{p}_i to solve (3), yielding the polynomial coefficients \mathbf{c} and thus the optimal polynomial trajectory. For dataset generation, We use MINCO [16] to connect the current states and the sampled relative waypoints \mathbf{p}_i via minimum-control polynomials. The waypoints \mathbf{p}_i and their corresponding durations T_i are extracted to form the dataset used to train the neural networks. Readers are referred to our previous work [31] for details of the time-allocation network applied to time-optimal planning.

In summary, this method can generate a dynamically feasible and near time-optimal trajectory in real time under polynomial representations. However, polynomial trajectory optimization is a relaxation of the time-optimal control problem for MAVs navigating through multiple waypoints, which inevitably leaves a non-negligible gap compared to true time-optimal navigation. This gap stems primarily from the inherent smoothness of finite-degree polynomials, which cannot fully exploit control inputs [23].

III. TIME-OPTIMAL MODEL PREDICTIVE CONTOURING CONTROL WITH COLLISION AVOIDANCE

This section presents a control method, referred to as MPCC, that tracks the reference trajectory in a truly time-optimal manner while accounting for the full quadrotor dynamics and obstacle avoidance.

A. Quadrotor Dynamics

The quadrotor's state space is expressed as $\mathbf{x} = [\mathbf{p}, \mathbf{q}, \mathbf{v}, \boldsymbol{\omega}]^T$, where $\mathbf{p} \in \mathbb{R}^3$ represents the position, $\mathbf{q} \in \mathbb{SO}(3)$ denotes the attitude quaternion, $\mathbf{v} \in \mathbb{R}^3$ is the linear velocity, and $\boldsymbol{\omega} \in \mathbb{R}^3$ represents the bodyrates in the body frame. The system inputs include the collective thrust \mathbf{F} and body torques $\boldsymbol{\tau}$. The dynamic equations are expressed as:

$$\begin{aligned}
\dot{\mathbf{p}} &= \mathbf{v}, \\
\dot{\mathbf{q}} &= \frac{1}{2} \mathbf{q} \odot \begin{bmatrix} 0 \\ \boldsymbol{\omega} \end{bmatrix}, \\
\dot{\mathbf{v}} &= \mathbf{g} + \frac{1}{m} \mathbf{R}(\mathbf{q}) \mathbf{F} - \mathbf{R}(\mathbf{q}) \mathbf{D} \mathbf{R}^T(\mathbf{q}) \cdot \mathbf{v}, \\
\dot{\boldsymbol{\omega}} &= \mathbf{J}^{-1} (\boldsymbol{\tau} - \boldsymbol{\omega} \times \mathbf{J} \boldsymbol{\omega})
\end{aligned} \tag{5}$$

where \odot represents Hamilton quaternion multiplication, $\mathbf{R}(\mathbf{q})$ is the quaternion rotation matrix, m is the quadrotor mass, \mathbf{J} is the inertia matrix, and $\mathbf{D} = \text{diag}(d_x, d_y, d_z)$ represents the drag coefficients [10].

Additionally, the input of \mathbf{F} and $\boldsymbol{\tau}$ is decomposed into individual rotor thrusts $\mathbf{f} = [f_1, f_2, f_3, f_4]$:

$$\mathbf{F} = \begin{bmatrix} 0 \\ 0 \\ \sum f_i \end{bmatrix}, \quad \text{and} \quad \boldsymbol{\tau} = \begin{bmatrix} \frac{l}{\sqrt{2}}(f_1 + f_2 - f_3 - f_4) \\ \frac{l}{\sqrt{2}}(-f_1 + f_2 + f_3 - f_4) \\ c_\tau(f_1 - f_2 + f_3 - f_4) \end{bmatrix} \tag{6}$$

where f_i is the thrust at rotor $i \in \{1, 2, 3, 4\}$, l represents the quadrotor's arm length and c_τ is the rotor's torque constant.

B. Time-Optimal MPCC Integrating with SFC

In contrast to solving trajectory planning and control separately, model predictive contouring control (MPCC) allows robust tracking of a continuously differentiable path while maximizing the traverse speed in a receding horizon fashion by solving the time allocation and control problems simultaneously in real time [26]. In time-critical scenarios, a time-optimal reference path (e.g., time-optimal point-mass model trajectory or time-optimal polynomial trajectory [31]) helps the MPCC find a good approximation of the time-optimal policy. For the MPCC, deviations from the reference path are permitted to enhance aggressiveness. Nevertheless, in cluttered environments, sacrificing tracking accuracy for time-optimal performance can result in unsafe flight trajectories. Thus, to ensure safety, this section proposes a variant MPCC to constrain a certain horizon of the predicted trajectory within the known free space based on SFC, enabling agile obstacle avoidance at a high replanning frequency, as shown in Fig. 5.

The contouring control problem transforms the trajectory to be tracked, parameterized by time, into an arc-length parameterized trajectory. The arc length of the reference path (or progress) is denoted as θ , with the arc length at timestep k denoted as θ_k . To incorporate the dynamics (5) within the MPCC formulation, the state space is augmented with progress dynamics by adding θ and progress speed v_θ as virtual states:

$$\bar{\mathbf{x}} = [\mathbf{p}, \mathbf{q}, \mathbf{v}, \mathbf{w}, \mathbf{f}, \theta, v_\theta]^T, \quad \bar{\mathbf{u}} = [\Delta \mathbf{f}, \Delta v_\theta]^T \tag{7}$$

where the progress acceleration Δv_θ is introduced as a virtual input, following typical contouring controller implementations [26], to avoid uncontrolled rapid change of v_θ , which would result in noisy control inputs. The dynamics of the augmented states are:

$$\dot{\mathbf{f}} = \Delta \mathbf{f}, \quad \dot{\theta} = v_\theta, \quad \dot{v}_\theta = \Delta v_\theta \tag{8}$$

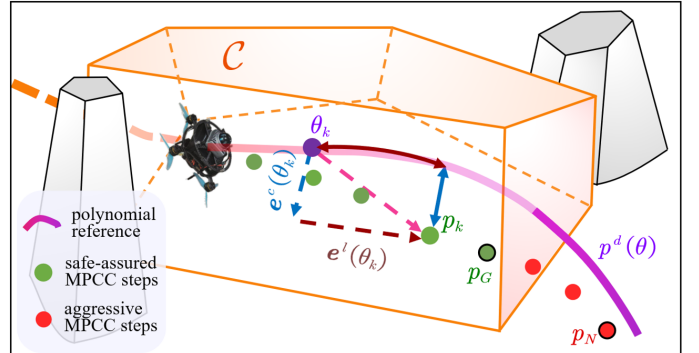


Fig. 5. 3D MPCC diagram with local SFC constraints applied to the first G steps to enable time-optimal flight while avoiding obstacles.

The MPCC problem is formulated as follows :

$$\begin{aligned}
\pi(\mathbf{x}) = \underset{\bar{\mathbf{u}}}{\text{argmin}} \sum_{k=0}^N & (\|e^l(\theta_k)\|_{q_l}^2 + \|e^c(\theta_k)\|_{q_c}^2 \\
& + \|\omega_k\|_{Q_\omega}^2 + \|\Delta \mathbf{f}_k\|_{R_{\Delta \mathbf{f}}}^2 + \|\Delta v_{\theta_k}\|_{R_{\Delta v}}^2 - \mu v_{\theta,k}) \\
\text{subject to} \quad & \mathbf{x}_0 = \bar{\mathbf{x}} \\
& \bar{\mathbf{x}}_{k+1} = \bar{\mathbf{x}}_k + d_t \cdot f(\bar{\mathbf{x}}_k, \bar{\mathbf{u}}_k) \\
& \omega_{min} \leq \omega \leq \omega_{max} \\
& \mathbf{f}_{min} \leq \mathbf{f} \leq \mathbf{f}_{max} \\
& 0 \leq v_\theta \leq v_{\theta,max} \\
& \Delta \mathbf{f}_{min} \leq \Delta \mathbf{f} \leq \Delta \mathbf{f}_{max} \\
& \Delta v_{\theta,min} \leq \Delta v_\theta \leq \Delta v_{\theta,max}
\end{aligned} \tag{9}$$

where the contour error $e^c(\theta_k)$ and lag error $e^l(\theta_k)$ represent the perpendicular and tangential errors between the position p_k and its projection on the reference path $p^d(\theta)$ at timestep k , as in Fig. 5. The q_c , q_l , and μ are the weights for the contour error, lag error, and progress term, respectively. N represents the prediction horizon, and $f(\bar{\mathbf{x}}_k, \bar{\mathbf{u}}_k)$ denotes the dynamics derived by discretizing (5) and (8) with time step d_t .

Although the waypoints generated in Section II-A are guaranteed to be obstacle-free, the resulting polynomial reference trajectories may still collide with obstacles, since no constraints are imposed on the trajectory segments between the waypoints. Moreover, due to the inherent trade-off between tracking accuracy and time optimality in MPCC, the resulting trajectory may deviate from the reference even when the reference itself is collision-free, potentially leading to collisions with obstacles. Furthermore, (1) optimistically assumes that unseen regions are obstacle-free. Thus, to ensure safety, the planned trajectory of the MPCC must be rigorously constrained to remain within the known free space. From point cloud data under partial environmental knowledge, it is guaranteed that a polytope \mathcal{C} extracted by CIRI remains entirely within the known free space, provided that the input point cloud forms a sufficiently dense depth image from LiDAR sensors and that the input seed includes the current MAV position [13]. Hence, similar to (1), a local SFC \mathcal{C} is qualified as a strict constraint for position \mathbf{p} to ensure safety:

$$\mathcal{C} = \{\mathbf{p} \in \mathbb{R}^3 \mid \mathbf{A}\mathbf{p} \leq \mathbf{b}\}, \quad \mathbf{A} \in \mathbb{R}^{m \times 3}, \quad \mathbf{b} \in \mathbb{R}^m \tag{10}$$

For each planning cycle, the naive idea is to directly incorporate the local SFC constraints \mathcal{C} into the MPCC predicted positions over the entire future horizon N . However, when unknown obstacles are detected during flight, environmental changes can cause frequent shrinking and expanding of the local SFC, which is particularly true during high-speed flight or in unstructured, dense environments. If SFC constraints are applied to the entire horizon, a suddenly narrowed SFC may result in its range being smaller than the MPCC's trajectory length. Thus, it may decrease global flight speed, leading to conservative performance. Moreover, as a well-known drawback of optimization-based controllers, imposing excessively tight constraints may undermine the solver's stability and success rate [32].

Considering the high replanning frequency and efficient time allocation of the proposed method, since MPC follows a receding-horizon scheme and applies only the first control input at each iteration, constraining the immediate state should guarantee that the quadrotors remain within the safe region. However, for real-time implementation, the MPCC employs an iterative scheme for computational efficiency, which requires multiple rolling iterations to obtain a feasible solution [33]. During runtime, constraining only the next-step state leads to suboptimal obstacle avoidance performance and may compromise safety. To strike a balance between aggressiveness and safety, we define $G < N$ as the safe horizon and only impose constraints on the first G steps of the MPCC:

$$\mathbf{A}\mathbf{p}_k \leq \mathbf{b}, \quad k \in \{1, \dots, G\} \quad (11)$$

where \mathbf{p}_k is the predicted position computed by MPCC at timestep k . By embedding (11) into (9), aggressive yet safe flight can be achieved, as depicted in Fig. 5.

For high-speed flight in partially known environments, the continuously updating map necessitates high-frequency replanning for obstacle avoidance. However, when the local SFC \mathcal{C} and front-end path are generated, the detection of previously unseen obstacles can lead to inconsistencies in path topology between consecutive planning loops, which may result in suboptimal or even unstable behavior of the MPC-based scheme. To address this issue, we propose a replanning method that ensures a smooth and consistent transition between trajectories generated in consecutive planning loops, which is called the **trajectory reuse** strategy. At current planning loop, the A* algorithm is initialized from p_G , which corresponds to the G -th state of the trajectory generated in the previous planning loop, while the states between the current state p_c and p_G are guaranteed to be safe by the SFC constructed in the previous loop (Fig. 6(a)). Moreover, since both p_c and p_G lie within the convex polytope of the previous SFC, which is obstacle-free by construction, they can be directly used as valid seeds for convex decomposition to generate the SFC \mathcal{C} for the current planning loop (Fig. 6(b)). This strategy ensures the consistency of the MPCC formulation across consecutive planning loops. The effectiveness of trajectory reuse is demonstrated via ablation studies in Section IV.

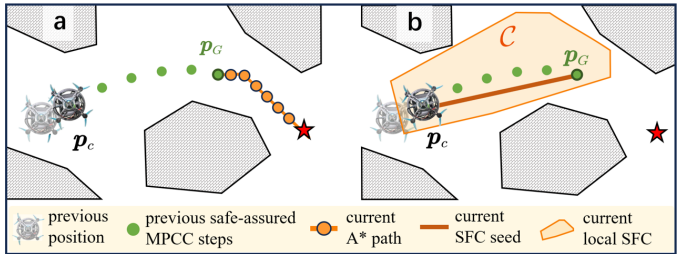


Fig. 6. Illustration of the strategy for maintaining consistency across two consecutive planning loops. (a) The A* algorithm is initialized from p_G , the G -th state of the trajectory generated in the previous planning loop. (b) The line segment connecting the current state p_c and p_G is used as the seed for generating the SFC.

TABLE I: Parameters in simulation & real world

Parameters	$diag(\mathbf{J}) [\text{gm}^2]$ [50,53,62]	$m [\text{kg}]$ 1.55	$l [\text{m}]$ 0.1125	$c_\tau [1]$ 0.02	$(d_x, d_y, d_z) [\text{s}^{-1}]$ (0.3,0.3,0.5)
Parameters	$\omega_{\text{max}} [\text{rad}\cdot\text{s}^{-1}]$ [10,10,0.3]	N 20	G 10	μ 500	q_c 30000

IV. EXPERIMENTS AND ANALYSIS

A. Simulation Experiments

1) *Experimental Setup*: The proposed approach is evaluated extensively through both simulation and real-world experiments. The basic parameters are kept consistent in both simulation and real-world experiments, as shown in Table I. The MPCC is deployed on acados [33], using SQP-RTI for real-time computation, with the control loop running at 100 Hz. We use a horizon length of $N = 20$ and a time step of $d_t = 0.03$ s. Online replanning is performed at every control loop, both on a desktop computer with an Intel i9-13900HX CPU for simulation and on the Intel NUC 13 with an i7-1360P CPU for experiment. The neural network is built and trained using the PyTorch framework and deployed using libtorch for real-time inference.

We benchmark LOONG against state-of-the-art planning frameworks for autonomous navigation. SUPER [13], a high-speed polynomial navigation framework, is selected for its suitability for time-critical tasks, while IPC [19] is included as a representative low-latency integrated planning-control baseline. We use two open-source simulation environments with different obstacle densities that focus on challenging flight in **time-critical task** (Fig. 7) or **cluttered forest** (Fig. 8), and the LiDAR simulator provided by SUPER, which considers the limited field of view (FOV) and realistic point of LiDAR sensor [13]. It should be noted that SUPER's simulator does not account for the MAV's dynamics, which assumes that SUPER's trajectories of $\mathbf{p}, \mathbf{q}, \mathbf{v}$ can be perfectly tracked. For the other two integrated planning-control frameworks, IPC uses a simplified third-order integrator assuming MPC states of $\mathbf{p}, \mathbf{v}, \mathbf{a}$ can be perfectly tracked with jerk j input. In contrast, ours incorporates an external integrator of full dynamics (7) with thrusts \mathbf{f} as inputs.

2) *Ablation Studies in Time-Critical Task Scenario*: We first conduct an ablation study in the **time-critical task** scenario based on the default configuration of LOONG to quantify how each component of our framework affects reliability and aggressiveness. Each configuration is evaluated over 10 trials

TABLE II: Ablation studies in the time-critical task.

Configuration	Number of Success ↑	Average Velocity (m/s) ↑	Average Maximum Velocity (m/s) ↑	Average Flight Time (s) ↓
Default ($G = 10$)	10/10	26.89	42.77	3.72
$G = 1$	6/10	26.61	40.46	3.76
$G = N = 20$	5/10	18.24	29.76	5.56
w.o. Trajectory Reuse	2/10	26.92	45.41	3.71
w.o. Passing SFC Intersection	1/10	24.65	37.88	4.05

with identical start and goal, and the success rate, average velocity, average maximum velocity, and average flight time are recorded in Table II, where averages are computed only over successful trials. The default configuration includes all modules described above with a mass-normalized collective thrust limit of $f_{max} = 33\text{m/s}^2$, which is evenly allocated to four individual thrusts as dynamic constraints in (9). Compared to the default configuration, where $G = 10$, **trajectory reuse** is enabled for replanning, and waypoints are selected by passing through the SFC intersections, we evaluate several variants by separately modifying these components, including configurations with $G = 1$ and $G = 20$, disabling **trajectory reuse**, and selecting waypoints without passing through the SFC intersections.

The results indicate that when $G = 1$, the insufficient real-time iterative solving undermines obstacle avoidance without improving flight speed. We conjecture that insufficient solver progress keeps the MPCC trajectory close to obstacles, thereby limiting the free space available for subsequent optimization. When $G = 20$, excessively strict and conservative constraints result in reduced aggressiveness and more solver failures. In the absence of **trajectory reuse**, the front-end A* may select kinetically infeasible or densely obstructed paths, which then lead to collisions or failures in the back-end MPCC. Without passing the SFC intersection, the success rates drop substantially, since the waypoints are placed too close to obstacles, severely restricting perception range and the feasible solution space for trajectory optimization in high-speed flight.

3) *Benchmark in Time-Critical Task Scenario*: To exhibit the effectiveness and aggressiveness of the proposed method, we benchmark LOONG against SUPER and IPC in **time-critical task** scenario encouraging aggressive maneuvering, as shown in Fig. 7, where four configurations are evaluated in the comparison. We respect the default configurations of the baseline methods, including the default SUPER, originally designed for MAVs with a thrust-to-weight ratio exceeding 5, and the default IPC. To ensure a fair comparison under identical actuator constraints, we configure both SUPER and LOONG with the same maximum collective thrust, $f_{max} = 25\text{m/s}^2$. For this comparison, all other dynamic constraints in SUPER, including velocity, acceleration, and jerk limits, are removed, while the maximum collective thrust in LOONG is reduced from its default configuration to match f_{max} . In addition, the default SUPER configuration is retained as a reference baseline. All methods are evaluated over 10 repeated trials.

The upper part of Table III records the success rates over repeated trials, computation time for planning and control, and etc. Since the obstacles in this scenario are relatively sparse, none of the methods experienced collisions or solver failures. Our method achieves greater aggressiveness in terms

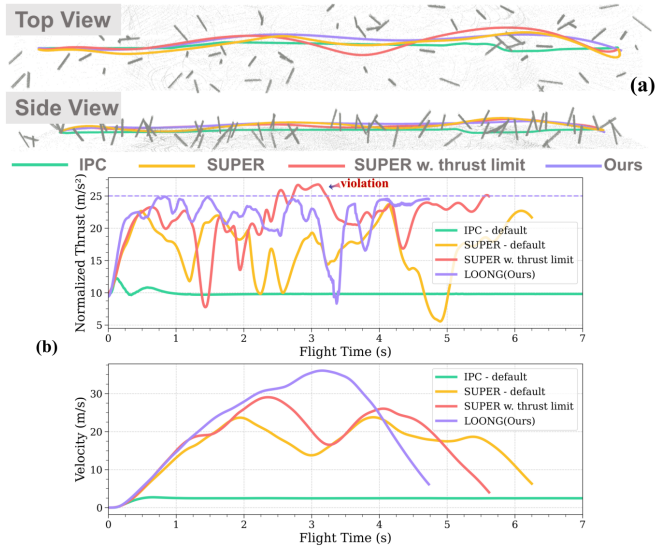


Fig. 7. One trial of four methods with identical start and goal points. (a) Trajectories in **time-critical task** simulation. (b) Mass-normalized collective thrust and velocity profiles. Our method fully exploits the thrust limit while maintaining obstacle avoidance.

of average velocity, average maximum velocity, and average flight time compared to other approaches, while maintaining comparable safety. As shown in Fig. 7(b), SUPER slightly exceeds the limit $f_{max} = 25\text{ m/s}^2$. We conjecture that, under a general multi-objective optimization framework, soft constraints can be violated [16]. Despite occasionally violating the thrust limit, SUPER still exhibits longer flight times than our LOONG. We attribute the reduced aggressiveness of SUPER primarily to two factors. First, SUPER plans polynomial trajectories, whose inherent smoothness conflicts with time-optimal objectives [23], fundamentally limiting achievable flight speed. Second, as SUPER prioritizes safety, it switches to conservative trajectories when high-speed replanning cannot be completed within the required time, which further reduces flight aggressiveness. In contrast, our method can reach the input limits without violation, ensuring that dynamic constraints are satisfied even when the MAV is operating at actuator limits, while achieving a replanning frequency of 100Hz, aligning with IPC in planning-control integration efficiency. Moreover, although IPC supports high planning frequency, it is overly conservative due to its naive average time allocation, and is therefore excluded from subsequent benchmarks.

4) *Benchmark in Cluttered Forest*: To evaluate the robustness of LOONG, we conduct experiments in the **cluttered forest** scenario and compare its performance with SUPER. For a fair comparison against SUPER’s two open-source configurations *high-speed* (default) and *dense*, the velocity limit of LOONG, $v_{\theta,max}$, is reduced from its default configuration to 25 m/s or 8 m/s, respectively, to match SUPER’s maximum speeds v . For each configuration, 10 trials are conducted with different start and goal points. The experimental results are summarized in the lower part of Table III and Fig. 8. Table III indicates that for *high-speed* configuration, LOONG achieves faster flights and higher success rates by leveraging actuators more sufficiently and maintaining a higher replanning frequency. For *dense* configuration, LOONG finishes all

TABLE III: Comparison of different framework in Simulation.

Scenario	Planning Framework	Number of Success \uparrow	Average Velocity (m/s) \uparrow	Average Maximum Velocity (m/s) \uparrow	Average Computation Time (ms) \downarrow	Average Flight Time (s) \downarrow
<i>time-critical task</i> 15m \times 120m \times 4m	SUPER - default	10/10	16.23	24.88	24.86	6.24
	IPC - default	10/10	2.85	3.19	2.41	40.57
	SUPER - w. only thrust limit	10/10	17.99	29.91	25.28	5.62
	LOONG(Ours)	10/10	22.10	33.15	5.87	4.64
<i>cluttered forest</i> 60m \times 60m \times 5m	SUPER - high-speed	4/10	7.34	17.63	47.98	8.81
	LOONG(Ours) - high-speed	6/10	13.63	20.60	6.84	4.56
	SUPER - dense	10/10	6.81	8.00	50.11	9.53
	LOONG(Ours) - dense	10/10	6.94	9.28	6.43	9.15

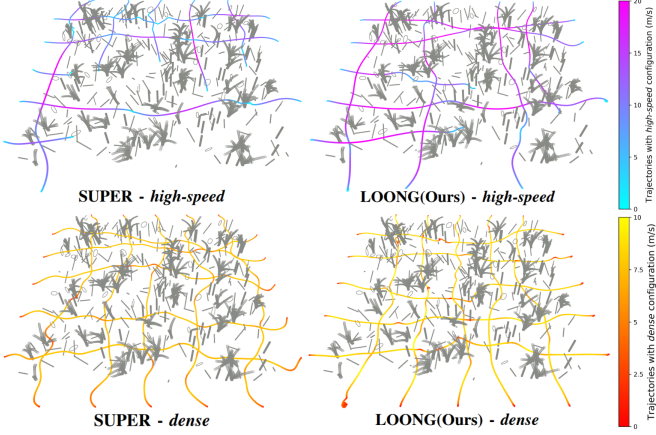


Fig. 8. Trajectories of four planning configurations starting from 10 different points in the *cluttered forest* scenario. Some *high-speed* trials failed while all *dense* trials succeeded. Ours achieved a more agile performance compared to SUPER.

flights while demonstrating superior agility and computational efficiency. Notably, compared to Section IV-A3, while SUPER manages *time-critical task* by *high-speed* configuration and *cluttered forest* by *dense* configuration, it necessitates extensive parameter tuning, such as planning horizon, penalty weights, resolution, etc., whereas LOONG requires only one parameter $v_{\theta,max}$ adjustment. Moreover, due to relatively stable MPCC complexity and consistent neural network inference time, LOONG’s computation time is largely insensitive to environmental complexity, 5.87 ms and 6.43 ms respectively, whereas SUPER’s computation time nearly doubles from 24.86 ms in *time-critical task* to 50.11 ms in *cluttered forest*.

B. Real-world Experiments

1) *Real-world Experiment Setup*: We validate the system’s effectiveness and reliability through real-world experiments. The experiments can be found in the [video]. For the hardware platform, we deploy a custom-built compact MAV with a 225 mm wheelbase, as shown in Fig. 9. The fully loaded vehicle weighs 1.5 kg and delivers a thrust-to-weight ratio exceeding 5.0. It is actuated by T-Motor F80PRO motors, which are typically used in racing drone, providing high thrust (up to 21.1 N with 5-inch propellers) and rapid response. The onboard computation is performed by an Intel NUC 13 computer featuring a 12-core 5.0 GHz CPU, and a flight control unit (FCU) running Betaflight with custom firmware. For perception, the MAV is equipped with a MID-360 3D LiDAR sensor. FAST-LIO2 [34] is used to fuse data from the

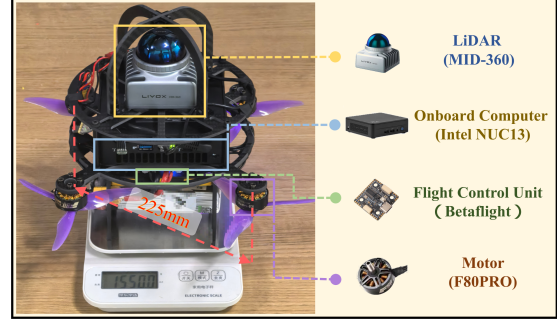


Fig. 9. Hardware platform of LOONG.

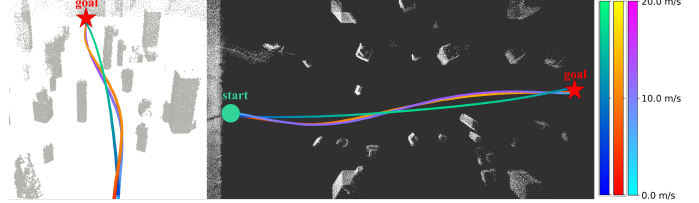


Fig. 10. Real-world trajectories visualization for repeated high-speed flights, demonstrating the reproducible aggressive behavior.

LiDAR and IMU sensors, while a sliding point-cloud map [13] is used to represent the occupied spaces of the environment. For planning and control, the default configuration of LOONG is used.

2) *High-Speed Autonomous Flights in Clutter*: To test the systematic effectiveness and aggressiveness of the proposed method, we first have our MAV perform an aggressive flight in a 20 m indoor scenario with obstacles. As shown in Fig. 1, the MAV begins at a hover height of 1.5 m at $t = 0$ s and traverses a 10 m \times 10 m cluttered region to reach the goal. The obstacle field has a density of 0.30 obstacles/m², with obstacle heights in the range [0.8 m, 3.0 m] and obstacle radii in the range [0.2 m, 0.6 m]. The maximum gap between adjacent obstacles is about 2.5 m. As shown in Fig. 1(b), the velocity profile indicates that the MAV reaches 18 m/s in about 1.2 s, while the throttle profile normalized by the collective thrust limit shows that the system can operate at its maximum thrust, enabling agile maneuvering among obstacles during the real-time autonomous flight. Three additional experiments are conducted to evaluate the robustness of the proposed system, as shown in Fig. 10.

3) *Consecutive Trials with Random Start Points*: As shown in Fig. 11, the MAV adaptively maneuvered through free space between obstacles in ten consecutive trials of 18 m forward flight, demonstrating the real-world generalization and reli-

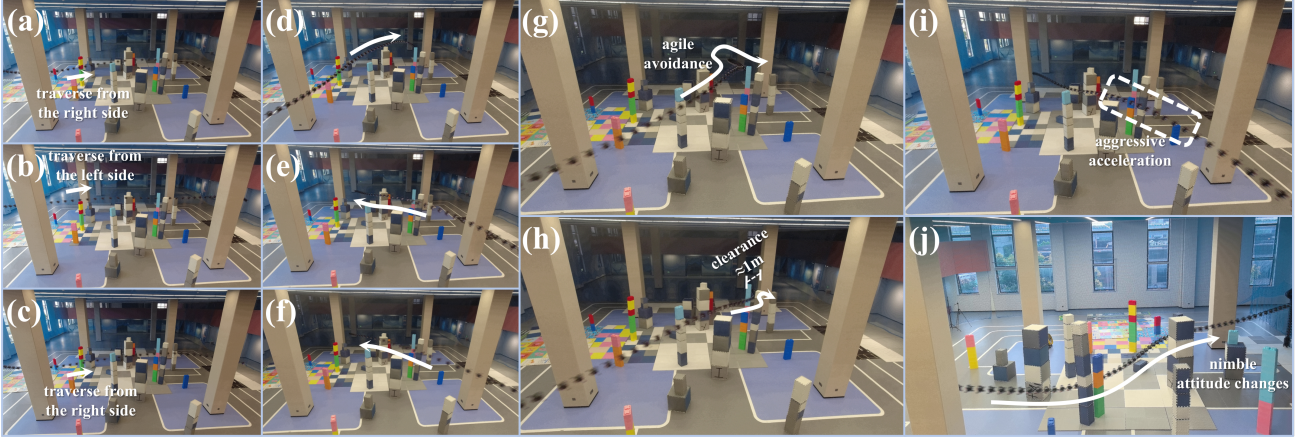


Fig. 11. Real-world trajectories from ten consecutive trials with random start points. Snapshots in the composite trajectory plot are taken at 0.033 s intervals. The MAV autonomously performs various obstacle avoidance behaviors: (a)-(c) bypassing obstacles at high speed from different sides, (d)-(f) gaining altitude to avoid densely cluttered regions, (g) aggressive avoidance maneuvers in response to close obstacles, (h) rapid traversal through a narrow gap, (i) large pitch maneuver for acceleration, (j) nimble attitude changes.

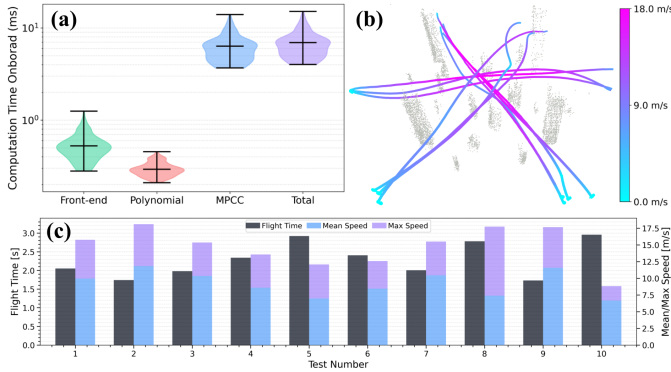


Fig. 12. Real-world consecutive trial data of LOONG. (a) Onboard computation time distribution per step, with total time below 10 ms to achieve 100 Hz replanning. (b) Visualization of ten trajectories. (c) Statistics of flight time and velocity.

bility of our system with the default LOONG configuration. The MAV traversed from three directions, with initial positions randomly selected within a 2 m radius and initial yaw angles within $\pm 10^\circ$. Fig. 12 presents the onboard computation time of each planning component per loop. It can be observed that the proposed path planning and reference generation methods require approximately 0.5 ms and 0.3 ms per loop, respectively, demonstrating high computational efficiency. By significantly reducing the computational burden of the front-end modules, sufficient onboard computational resources are reserved for the more time-consuming MPCC, thereby enabling the MAV to achieve online planning at a frequency of 100 Hz. Despite traversing highly cluttered obstacles, all ten consecutive flights succeed, as depicted in Fig. 12(b), and achieved an average peak speed of 14.72 m/s and an average flight time of 2.29 s, as illustrated in Fig. 12(c). These results strongly demonstrate our framework's capability to autonomously generate safe and agile trajectories in challenging environments in real time.

V. CONCLUSION AND DISCUSSION

This article presents a learning-accelerated online time-optimal planning and control framework termed LOONG for MAVs' high-speed autonomous flight, which exhibits both

aggressive flight performance and safety in simulation and real-world experiments. Several improvements are envisioned for future work. For the optimization scheme, while the current RTI solver enables real-time performance, its convergence may be challenged in extremely dynamic environments. The recent advancement of onboard GPUs and the sampling-based scheme of model predictive path integral (MPPI) could overcome this bottleneck by enabling massive parallel rollouts in real time. Moreover, our benchmark demonstrates LOONG's generalization by merely adjusting the maximum progress speed. Thereby, environment-adaptive tuning remains a promising enhancement. Finally, given LOONG's fully autonomous design and generalization, expanding its application to outdoor and field environments offers an exciting frontier for achieving even greater performance.

REFERENCES

- [1] Y. Zhou, S. Lai, H. Cheng, A. H. M. Redhwan, P. Wang, J. Zhu, Z. Gao, Z. Ma, Y. Bi, F. Lin, and B. M. Chen, "Toward autonomy of micro aerial vehicles in unknown and global positioning system denied environments," *IEEE Transactions on Industrial Electronics*, vol. 68, DOI 10.1109/TIE.2020.3008378, no. 8, pp. 7642–7651, 2021.
- [2] R. Li and B. Xin, "Autonomous navigation of quadrotors in dynamic complex environments," *IEEE Transactions on Industrial Electronics*, vol. 72, DOI 10.1109/TIE.2024.3433585, no. 3, pp. 2790–2800, 2025.
- [3] K. Liu and B. M. Chen, "Industrial uav-based unsupervised domain adaptive crack recognitions: From database towards real-site infrastructural inspections," *IEEE Transactions on Industrial Electronics*, vol. 70, DOI 10.1109/TIE.2022.3204953, no. 9, pp. 9410–9420, 2023.
- [4] B. Mishra, D. Garg, P. Narang, and V. Mishra, "Drone-surveillance for search and rescue in natural disaster," *Computer Communications*, vol. 156, pp. 1–10, 2020.
- [5] S. M. S. M. Daud, M. Y. P. M. Yusof, C. C. Heo, L. S. Khoo, M. K. C. Singh, M. S. Mahmood, and H. Nawawi, "Applications of drone in disaster management: A scoping review," *Science & Justice*, vol. 62, no. 1, pp. 30–42, 2022.
- [6] H. Moon, J. Martinez-Carranza, T. Cieslewski, M. Faessler, D. Falanga, A. Simovic, D. Scaramuzza, S. Li, M. Ozo, C. De Wagter *et al.*, "Challenges and implemented technologies used in autonomous drone racing," *Intelligent Service Robotics*, pp. 1–12, 2019.
- [7] D. Hanover, A. Loquercio, L. Bauersfeld, A. Romero, R. Penicka, Y. Song, G. Cioffi, E. Kaufmann, and D. Scaramuzza, "Autonomous drone racing: A survey," *IEEE Transactions on Robotics*, 2024.
- [8] C. Richter, A. Bry, and N. Roy, "Polynomial trajectory planning for aggressive quadrotor flight in dense indoor environments," in *Robotics Research: The 16th International Symposium ISRR*, pp. 649–666. Springer, 2016.

[9] D. Mellinger and V. Kumar, "Minimum snap trajectory generation and control for quadrotors," in *2011 IEEE International Conference on Robotics and Automation*, pp. 2520–2525. IEEE, 2011.

[10] M. Faessler, A. Franchi, and D. Scaramuzza, "Differential flatness of quadrotor dynamics subject to rotor drag for accurate tracking of high-speed trajectories," *IEEE Robotics and Automation Letters*, vol. 3, no. 2, pp. 620–626, 2017.

[11] H. Oleynikova, M. Burri, Z. Taylor, J. Nieto, R. Siegwart, and E. Galceran, "Continuous-time trajectory optimization for online uav replanning," in *2016 IEEE/RSJ international conference on intelligent robots and systems (IROS)*, pp. 5332–5339. IEEE, 2016.

[12] K. Mohta, M. Watterson, Y. Mulgaonkar, S. Liu, C. Qu, A. Makineni, K. Saulnier, K. Sun, A. Zhu, J. Delmerico *et al.*, "Fast, autonomous flight in gps-denied and cluttered environments," *Journal of Field Robotics*, vol. 35, no. 1, pp. 101–120, 2018.

[13] Y. Ren, F. Zhu, G. Lu, Y. Cai, L. Yin, F. Kong, J. Lin, N. Chen, and F. Zhang, "Safety-assured high-speed navigation for mavs," *Science Robotics*, vol. 10, no. 98, p. eado6187, 2025.

[14] B. Zhou, F. Gao, L. Wang, C. Liu, and S. Shen, "Robust and efficient quadrotor trajectory generation for fast autonomous flight," *IEEE Robotics and Automation Letters*, vol. 4, no. 4, pp. 3529–3536, 2019.

[15] X. Zhou, X. Wen, Z. Wang, Y. Gao, H. Li, Q. Wang, T. Yang, H. Lu, Y. Cao, C. Xu *et al.*, "Swarm of micro flying robots in the wild," *Science Robotics*, vol. 7, no. 66, p. eabm5954, 2022.

[16] Z. Wang, X. Zhou, C. Xu, and F. Gao, "Geometrically constrained trajectory optimization for multicopters," *IEEE Transactions on Robotics*, vol. 38, no. 5, pp. 3259–3278, 2022.

[17] Y. Ren, F. Zhu, W. Liu, Z. Wang, Y. Lin, F. Gao, and F. Zhang, "Bubble planner: Planning high-speed smooth quadrotor trajectories using receding corridors," in *2022 IEEE/RSJ International Conference on Intelligent Robots and Systems (IROS)*, pp. 6332–6339. IEEE, 2022.

[18] G. Lu, W. Xu, and F. Zhang, "On-manifold model predictive control for trajectory tracking on robotic systems," *IEEE Transactions on Industrial Electronics*, vol. 70, DOI 10.1109/TIE.2022.3212397, no. 9, pp. 9192–9202, 2023.

[19] W. Liu, Y. Ren, and F. Zhang, "Integrated planning and control for quadrotor navigation in presence of suddenly appearing objects and disturbances," *IEEE Robotics and Automation Letters*, vol. 9, no. 1, pp. 899–906, 2023.

[20] J. Yuan, D. Cao, J. Mei, J. Chen, and S. Li, "Safety-critical online quadrotor trajectory planner for agile flights in unknown environments," in *2025 IEEE International Conference on Robotics and Automation (ICRA)*, pp. 11 773–11 779. IEEE, 2025.

[21] A. Loquercio, E. Kaufmann, R. Ranftl, M. Müller, V. Koltun, and D. Scaramuzza, "Learning high-speed flight in the wild," *Science Robotics*, vol. 6, no. 59, p. eabg5810, 2021.

[22] Y. Zhang, Y. Hu, Y. Song, D. Zou, and W. Lin, "Back to newton's laws: Learning vision-based agile flight via differentiable physics," *arXiv preprint arXiv:2407.10648*, 2024.

[23] P. Foehn, A. Romero, and D. Scaramuzza, "Time-optimal planning for quadrotor waypoint flight," *Science Robotics*, vol. 6, no. 56, p. eabh1221, 2021.

[24] Y. Song, A. Romero, M. Müller, V. Koltun, and D. Scaramuzza, "Reaching the limit in autonomous racing: Optimal control versus reinforcement learning," *Science Robotics*, vol. 8, no. 82, p. eadg1462, 2023.

[25] E. Kaufmann, L. Bauersfeld, A. Loquercio, M. Müller, V. Koltun, and D. Scaramuzza, "Champion-level drone racing using deep reinforcement learning," *Nature*, vol. 620, no. 7976, pp. 982–987, 2023.

[26] A. Romero, S. Sun, P. Foehn, and D. Scaramuzza, "Model predictive contouring control for time-optimal quadrotor flight," *IEEE Transactions on Robotics*, vol. 38, no. 6, pp. 3340–3356, 2022.

[27] A. Romero, R. Penicka, and D. Scaramuzza, "Time-optimal online replanning for agile quadrotor flight," *IEEE Robotics and Automation Letters*, vol. 7, no. 3, pp. 7730–7737, 2022.

[28] H. Oleynikova, Z. Taylor, M. Fehr, R. Siegwart, and J. Nieto, "Voxblox: Incremental 3d euclidean signed distance fields for on-board mav planning," in *2017 IEEE/RSJ International Conference on Intelligent Robots and Systems (IROS)*, pp. 1366–1373. IEEE, 2017.

[29] Q. Wang, Z. Wang, M. Wang, J. Ji, Z. Han, T. Wu, R. Jin, Y. Gao, C. Xu, and F. Gao, "Fast iterative region inflation for computing large 2-d/3-d convex regions of obstacle-free space," *IEEE Transactions on Robotics*, 2025.

[30] S. Liu, M. Watterson, K. Mohta, K. Sun, S. Bhattacharya, C. J. Taylor, and V. Kumar, "Planning dynamically feasible trajectories for quadrotors using safe flight corridors in 3-d complex environments," *IEEE Robotics and Automation Letters*, vol. 2, no. 3, pp. 1688–1695, 2017.

[31] X. Guan, F. Zhao, S. Tian, and S. Li, "Learning time-optimal online replanning for distributed model predictive contouring control of quadrotors," in *2025 IEEE International Conference on Robotics and Automation (ICRA)*, pp. 14 527–14 533. IEEE, 2025.

[32] J. Kohler, M. A. Müller, and F. Allgower, "Analysis and design of model predictive control frameworks for dynamic operation—an overview," *Annual Reviews in Control*, vol. 57, DOI <https://doi.org/10.1016/j.arcontrol.2023.100929>, p. 100929, 2024.

[33] R. Verschueren, G. Frison, D. Kouzoupis, J. Frey, N. v. Duijkeren, A. Zanelli, B. Novoselnik, T. Albin, R. Quirynen, and M. Diehl, "acados—a modular open-source framework for fast embedded optimal control," *Mathematical Programming Computation*, vol. 14, no. 1, pp. 147–183, 2022.

[34] W. Xu, Y. Cai, D. He, J. Lin, and F. Zhang, "Fast-lio2: Fast direct lidar-inertial odometry," *IEEE Transactions on Robotics*, vol. 38, DOI 10.1109/TRO.2022.3141876, no. 4, pp. 2053–2073, 2022.